Thermochemical CO2 Splitting Using Double Perovskite-Type Ba2Ca0.66Nb1.34-xFexO6-δ

S, Mulmi; C, haomin; A, Hassan; J.F., marco; Berry, Frank; F, Sharif; Slater, Peter; E, Roberts; S, Adams; Thangaurai, V

DOI:
10.1039/C6TA10285A

Document Version
Peer reviewed version

Published in J. Mater. Chem A.

http://pubs.rsc.org/en/content/articlelanding/2017/ta/c6ta10285a#!divAbstract

Thermochemical CO_2 Splitting Using Double Perovskite-Type $Ba_2Ca_{0.66}Nb_{1.34-x}Fe_xO_{6-\delta}$

S. Mulmi,[a] C. Haomin,[b] A. Hassan,[c] J. F. Marco,[d] F. J. Berry,[e] F. Sharif,[c] P. R. Slater,[e] E. Roberts,[c] S. Adams[b] and V. Thangadurai*[a]

[a]*Department of Chemistry, University of Calgary, 2500 University Drive NW, Calgary, AB, T2N-1N4, Canada*

[b]*Department of Materials Science and Engineering, National University of Singapore, Singapore*

[c]*Department of Chemical and Petroleum Engineering, University of Calgary, 2500 University Drive NW, Calgary, AB, T2N-1N4, Canada*

[d]*Instituto de Química Física "Rocasolano", Consejo Superior de Investigaciones Cientificas, Serrano 119, 28006 Madrid, Spain*

[e]*School of Chemistry, The University of Birmingham, Birmingham B15 2TT, United Kingdom*

Corresponding author:* Venkataraman Thangadurai; vthangad@ucalgary.ca; Tel.: +1(403)-210-8649

Abstract

A carbon-neutral fuel is desired when it comes to solve the issues associated with climate change. A smart approach would be to develop new materials to produce such fuels, which could be integrated with renewables to improve the efficiency (e.g., solid oxide fuel cells (SOFCs) in smart grid, concentrated solar fuel technologies). In this study, we report the utilization of nonstoichiometric perovskite oxides, $Ba_2Ca_{0.66}Nb_{1.34-x}Fe_xO_{6-\delta}$ (BCNF) ($0 \leq x \leq 1$), to split CO_2 into carbon, carbon monoxide, and oxygen at elevated temperature. Powder X-ray diffraction shows the stability of double perovskite-type $Ba_2Ca_{0.66}Nb_{1.34-x}Fe_xO_{6-\delta}$ (BCNF) ($0 \leq x \leq 1$) after exposing to 2000 ppm CO_2 in Ar at 700 °C. Scanning electron microscopy coupled with energy dispersive X-ray, Raman spectroscopy, temperature programmed oxidation (TPO) and mass spectroscopy (MS), and DFT analyses confirm the formation of solid carbon upon CO_2 exposure, which increases with increasing Fe in BCNF. Mössbauer spectroscopy of as-prepared BCNF shows the presence of Fe^{3+}, Fe^{4+} and Fe^{5+}. Upon Ar exposure, the higher valent Fe component is

reduced to Fe^{3+} and subsequent oxidation of Fe^{3+} seems to promote the CO_2 reduction. Overall, these promising results of BCNFs, displaying redox activity at significantly lower temperatures compared to state-of-art ceria for CO_2 reduction, show great potential for their use in renewable-driven fuel technologies.

1. Introduction

CO_2 emission from fossil fuel combustion has been considered as a major threat for climate change. At present, over 75% of world energy demand is generated using fossil fuels, which releases large amounts of CO_2 and will continue to rise unless major steps are taken to mitigate CO_2 emissions. Among other greenhouse gases, CO_2 is a highly stable molecule and is very difficult to be converted into other useful chemicals. However, a large number of chemical manufacturing processes have also been developed for converting CO_2 into useful fuels such as $CO + H_2$ and CO. Furthermore, electrochemical methods have been considered to convert CO_2 into valuable chemicals, including CO,[1,2] methanol,[3,4] ethanol,[5] and formaldehyde.[6] Most of these methods are energy intensive and also require ultra-high pure CO_2. CO_2 is photochemically reduced to store energy by natural processes; mimicking this process remains one of the great challenges in modern chemistry.[7,8] It is commonly understood that the critical hindrance is to activate CO_2 into the $CO_2^{\bullet}$ radical intermediates that can be reconverted further into useful fuels. Currently, many electrocatalysts based upon metal oxide-derived nanostructured materials have been investigated intensely to lower the over-potential for CO_2 reduction.[9-12]

Here, we report a thermochemical splitting of CO_2 using a mixed ion and electron conducting (MIEC) perovskite-type $Ba_2Ca_{0.66}Nb_{1.34-x}Fe_xO_{6-\delta}$ (BCNF), where solid carbon was deposited along with the production of CO and oxygen. The pretreatment of BCNF followed by CO_2 conversion both were performed at significantly lower temperature (700 °C) compared to

conventional metal oxides that operate at 1200-1400 ^{o}C.[13-16] Additionally, we have not used any external potential difference to drive the CO_2 conversion reaction – making BCNF a highly promising alternative for renewable-derived carbon-neutral fuel production at significantly lower temperatures compared to state-of-art materials.[13-19] In particular, this discovery could have potential applications to regenerate low-cost fuels by integrating with solar energy to provide the heat source for the thermochemical process.

2. Experimental

Perovskite-type $Ba_2Ca_{0.66}Nb_{1.34-x}Fe_xO_{6-\delta}$ (BCNF) (x = 0, 0.34, 0.66 and 1) were prepared through a conventional solid-state reaction at elevated temperature in air using stoichiometric amounts of $BaCO_3$ (99+%, Alfa Aesar), $CaCO_3$ (99%, Fisher Scientific Company), Nb_2O_5 (99.5%, Alfa Aesar) and Fe_2O_3 (99+%, Alfa Aesar). These precursor powders were mixed together in an appropriate amount of ethanol (typically ~15-20 mL) followed by ball-milling (Pulverisette, Fritsch, Germany). The obtained mixture was calcined in air at 1000 °C and resultant powders were ball-milled again for 4 h and dried in air. The powders were pressed into pellets by applying in isotactic pressure of 200 MPa. The pressed pellets were sintered at 1400 °C using a high-temperature furnace (Carbolite RHF16/3, England) in air.

Powder X-ray diffraction (PXRD) (Bruker D8 Advance; Cu Kα, 40 kV and 40 mA; 0.02° step scan width and 6s counting time per step) was performed to confirm the formation of double perovskite-type structure for BCNF. BCNF pellets were crushed and ground into a fine powder for PXRD measurements. Scanning electron microscopy (SEM) (Philips XL30 SEM) was used to study the microstructure of the BCNF pellets. Temperature programmed oxidation (TPO) of BCNF samples was carried out in a CHEMBET 3000 (Quantachrome Instruments) instrument for as-prepared and CO_2-treated samples. BCN and BCNF samples were pre-treated with Ar (5.0

grade from Praxair, Canada) (O_2 content ~1 ppm) for 12 h at 700 °C prior to exposing CO_2 gas. He gas (UHP grade from Praxair, Canada) was purged at 15 cc/min before oxidation at ambient temperatures for 30 min. The sample was then heated up to 900 °C (10 °C/min) under 5% O_2 in He atmosphere flowing at 20 cc/min. The gases consumed (O_2) or produced (CO_2 and H_2O) were monitored using thermal conductivity detector (TCD) and mass spectroscopy (MS).

^{57}Fe Mössbauer spectra were recorded at 298 K in constant acceleration mode using a *ca.* 25mCi ^{57}Co/Rh source and a helium closed-cycle cryorefrigerator. All the spectra were computer fitted and the chemical isomer shift data are quoted relative to metallic iron at room temperature. Raman measurements were recorded in backscattering geometry on selected planes of the single crystals using a DILOR XY spectrometer with excitation through an X50 microscope objective lens. Entrance and exit polarizers were used to minimize polarization losses.

All *ab initio* calculations of the (100) surface of BCNF and the adsorption of CO_2 to this surface are performed using Vienna Ab initio Simulation Package (VASP),[20] with the PBE class of generalized gradient approximation (GGA-PBE) exchange-correlation potentials.[21] For calculating the energy of a structure, a relaxation is first performed at an energy cutoff of 400 eV with a k-mesh of 1×1×1, and then energy values are read from a single-point calculation with a denser k-mesh of 3×3×1. The DFT+U[22] scheme is applied both to obtain more accurate results as well to facilitate convergence. The U value for Fe ions is set to be 4.9,[23] while the U value for Nb is set to 2.0.[24,25] To set up a surface model, the experimentally determined bulk structure is used to create a 1×1×2 super-cell fixing the two bottom layers with experimental lattice parameters as well as atomic positions, while the two top layers are allowed to relax. A vacuum slab of 10Å thickness is inserted above the top layer in order to minimize the effect of periodic boundary conditions along the c-axis. The composition of the compound with all sites occupied

is set to be $Ba_{16}Ca_4Nb_7Fe_5O_{48}$ ($Ba_2Ca_{0.5}Nb_{0.875}Fe_{0.625}O_6$) corresponding to x = 0.625 and δ = 0. Due to the nature of mixed occupancy in this material, on any site of mixed occupancy one type of cation is assigned randomly, with a probability equal to the chosen occupancy, while keeping the stoichiometric ratio close to the bulk value.

3. Results and discussion

3.1. Structure and Phase Stability

All as-prepared $Ba_2Ca_{0.66}Nb_{1.34-x}Fe_xO_{6-\delta}$ (BCNF) (x = 0, 0.34, 0.66 and 1) samples exhibited a double perovskite-type cubic structure (space group: *Fm-3m*),[26] as confirmed using powder X-ray diffraction (Fig. S1). The double-perovskite structure of $Ba_2Ca_{0.66}Nb_{0.68}Fe_{0.66}O_{6-\delta}$ (BCNF66) and $Ba_2Ca_{0.66}Nb_{0.34}FeO_{6-\delta}$ (BCNF100) remained the same upon treating with 2000 ppm CO_2 in Ar for 24 h at 700 °C, while under pure CO_2 BCNF100 showed extra diffraction peaks due to $BaCO_3$ (Joint Committee on Powder Diffraction Standards (JCPDS) Card No. 05-0378), Fe_2C (JCPDS Card No. 36-1249), C (JCPDS Card No. 26-1080) and Fe_3O_4 (JCPDS Card No. 26-1136) (Fig. S1B). Details on reaction products are provided in Table S1. In contrast, BCNF66 showed no change in its original structure even with pure CO_2 exposure under the same conditions (Fig. S1A). Typical scanning electron microscopy (SEM) images coupled with energy dispersive X-ray (EDX) analysis of as prepared and CO_2-treated BCNF are shown in Figure 1. Deposition of C with the addition of 0.3 % CO_2 in Ar for all Fe-doped BCNFs, except the Fe-free parent compound, $Ba_2Ca_{0.66}Nb_{1.34}O_6$, is noticeably visible, suggesting that the dopant Fe is crucial for CO_2 reduction. Note that all as-prepared samples were pre-treated with Ar (5.0 grade, Praxair, Canada) in similar conditions (700 °C, 12 h) prior to introducing CO_2 into the system. The highest amount of C deposition was observed under pure CO_2 (Figs. 1J-L), when compared to ppm level CO_2 under the similar duration of CO_2 exposure (Figs. 1F-H). Selected area EDX

study shows the formation of C on all Fe-doped BCNFs. The x = 1 member, $Ba_2Ca_{0.66}Nb_{0.34}FeO_{6-\delta}$, exhibits higher C deposition on its surface compared to other BCNF members under all the investigated conditions. To substantiate the role of Fe in BCNFs for the conversion of CO_2 to C, a blank test with quartz glass (our gas-tight heating chamber) was done with pure CO_2 under similar conditions as was done for all BCNFs (700 °C for 24 h). The SEM/EDX results of quartz glass before and after exposing CO_2 are shown in Fig. S2 and confirm no C formation on it. As these MIECs were initially studied as *p*-type CO_2 gas sensors,[26,27] we anticipated interesting results on the formation of C by applying an external voltage (~100 mV). However, no differences were found between the Fe-doped BCNF66s, with and without applying any external potential difference, regarding the C formation on its surface (Fig. S3), suggesting that the observed CO_2 reduction is a thermochemical reduction.

3.2. Temperature-programmed oxidation (TPO) analysis on CO_2 treated BCNF.

The deposition of C was further verified using temperature-programmed oxidation (TPO) of CO_2-treated BCNF samples. Figure 2 shows typical TPO data for the x = 0.34, x = 0.66 and x = 1 members of $Ba_2Ca_{0.66}Nb_{1.34-x}Fe_xO_{6-\delta}$. The minima in thermal conductivity detector (TCD) signal at around 600 °C (~48 mins in Fig. 2A) correspond to oxidation, which is likely due to Fe in the presently studied system. The maxima in TCD after 640 °C (~52 mins. in Fig. 2A) indicate CO_2 gas that is evolved during the oxidation of C present in the BCNF. According to the CO_2 signal in MS results (Fig. 2B), the initial peak at ~400 °C (~30 mins) for BCNF100 (blue line) can be ascribed to amorphous carbon, whereas x = 0.34 and x = 0.66 members in BCNFs exhibit mostly graphitic carbon.[28] The amount of evolved CO_2 as assessed from the peak area in Fig. 2A indirectly shows the total amount of coke deposited while passing pure CO_2 prior to TPO-MS measurement. Among BCNFs, BCNF with x = 1 member, $Ba_2Ca_{0.66}Nb_{0.34}FeO_{6-\delta}$ (BCNF100),

exhibited the highest C deposition (Fig. 2C) even though partial decomposition occurs for this phase under pure CO_2. TPO-MS data illustrated in Fig. S4 agree with SEM/EDX and PXRD results indicating that even ppm levels of CO_2 can thermochemically dissociate on the surface of Fe-doped $Ba_2Ca_{0.66}Nb_{1.34-x}Fe_xO_{6-\delta}$. The BCNF66 member (x = 0.66 in BCNF), that exhibited good chemical stability under CO_2, shows the oxidation of C to CO_2 after 650 °C from the real-time mass spectrometry (MS) measurements coupled with TPO. This result displays that most of the carbon formed during ppm level CO_2 treatment on BCNF66 is graphitic carbon, which enhances the electrical conductivity, and hence, the change in the conductivity could be correlated to $p(CO_2)$.[27]

For further confirmation on the effect of Fe content in BCNF, TPO and MS are carried out simultaneously. Figure 3A shows the TCD signals for TPO measurements, whereas the corresponding real-time MS data is illustrated as Figure 3B. Note that all samples were pre-treated with Ar at 700 °C before being exposed to CO_2. The green line represents the Fe-free $Ba_2Ca_{0.66}Nb_{1.34}O_6$ (BCN) pre-treated with pure CO_2, where no signal related to CO_2 is observed under TPO (Fig. 3A) and MS data (Fig. 3B). These TPO-MS results signify that no coke formation occurred while performing pre-treatment of the sample with pure CO_2. For comparison, Fe-doped BCNF66 was also subjected to the same TPO-MS test. The TPO-MS signals in Figure 3B exhibit two peaks (red line) ascribed to CO_2 signals at 415 °C and 725 °C. For comparison, the data for as-prepared BCNF66 (without any CO_2 treatment) are shown by the blue line. In the latter case, the TPO and MS signals show no traces of CO_2 on heating up to 900 °C, thus indicating that as-prepared BCNF66 does not have any carbon, as compared to CO_2 pre-treated BCNF66 and thus indicating that coking occurs only after introducing CO_2 at elevated temperature.

3.3. ^{57}Fe Mössbauer spectroscopy and Raman spectroscopy

To understand the role of Fe on CO_2 reduction and the nature of the carbon, ^{57}Fe Mössbauer spectroscopy and Raman spectroscopy were performed. ^{57}Fe Mössbauer spectra recorded for as-prepared BCNF materials were best fitted to two quadrupole split absorptions together with single line absorption of low intensity (Fig. 4). The doublet with chemical isomer shift of *ca.* -0.08 mm s^{-1} is characteristic of Fe^{5+} in perovskite-related structures.[29-34] The doublet with chemical isomer shift *ca.* 0.16 mm s^{-1} is typical of Fe^{3+} in lower than octahedral coordination.[35] The singlet of low intensity with chemical isomer shift *ca.* 0.05 mm s^{-1} can be associated with Fe^{4+}.[35] This co-existence of Fe^{5+} and Fe^{3+} in perovskite-related phases of composition $Sr(Fe/M)O_3$ (M = Sn, Si) has been observed and attributed to disproportionation of Fe^{4+}.[32-34] A comparison of the data between samples with different Fe contents shows that the amount of Fe^{5+}, and hence average Fe oxidation state, increases with increasing iron concentration in the samples. Thus, it appears that Fe oxidation is favored as the Nb content is lowered, which can be correlated with the fact that the replacement of Nb^{5+} by Fe^{3+} would be expected to be accompanied by the introduction of oxygen vacancies within the structure and, to limit these anion vacancies, Fe would therefore be expected to adopt an increasingly higher average oxidation state as the Fe concentration increases. A schematic diagram of the replacement of Nb^{5+} by Fe^{3+} is illustrated in Figure 5. The chemical isomer shift of the Fe^{3+} component is lower than that normally encountered for Fe^{3+} in octahedral coordination, which is consistent with the presence of oxygen vacancies around the Fe^{3+} sites leading to a lower coordination number.

Raman spectra of as-prepared BCN and BCNFs were measured before (Fig. 6A) and after (Fig. 6B) CO_2-treatment at 700 °C for 24 h. All Fe-doped BCNF samples displayed peaks related to carbon and carbonates, whereas Fe-free BCN ($Ba_2Ca_{0.66}Nb_{1.34}O_6$) showed no peaks between

1000 cm^{-1} to 2000 cm^{-1}. The D-band (disorder-induced mode) in CO_2-treated BCNFs is due to the disordered-type graphitic carbonaceous species at *ca.* 1360 cm^{-1} in the Raman spectrum (Fig. 6B).[36,37] The D-bands due to the breathing vibrational mode of six- membered carbon rings are observed in the frequency range of 1350-1430 cm^{-1},[38] suggesting graphitic-like carbon formation. The disorder-induced character of the D band is clearly observed in Figure 6E, which shows few bright spots (~1μm) in Raman images of disordered graphitic carbon deposited on BCNF66 after CO_2-treatment (#1 and #3). However, the relatively darker spots (#2 and #4) near brighter ones in CO_2-treated BCNF66 suggested that the formation of carbon occurs randomly on the material's surface. In the next step, the CO_2-treated BCNF66 was further oxidized at 900 °C for 12 h and the Raman spectra was analyzed again, where no traces of carbon were detected as anticipated from previous SEM/EDX and TPO-MS data. The sample with the maximum Fe incorporation in BCNF (*i.e.* BCNF100) yields an additional peak at 1087 cm^{-1} (Fig. 6B) that refers to the carbonate ion vibration.[39] SEM/ EDX data on BCNFs also agree with this result, where we see new phase formation, possibly alkaline earth carbonates, leading to many cracks on the surface (Fig. S5). The images for BCNFs before CO_2-treatment were also taken using Raman spectroscopy measurement. The images for Fe-free BCN (x = 0) (Fig. S6A), and BCNF with x = 0.33 (Fig. S6B), x = 0.66 (Fig. S6C), and x = 1 (Fig. S6D) showed no carbon deposition on their surface. In contrast, BCNF66 exposed to pure CO_2 appeared to have carbon deposited on its surface (Figs. S6E, F).

3.4. Possible Mechanism of CO_2 reduction on BNCF

The key result of this study is the observation of the thermochemical reduction of CO_2 to C, where the process is facilitated by the presence of Fe (the level of C formation increases with increasing Fe content). In addition to the production of C, the mechanism of CO_2 splitting also

involved CO and O_2 as products (Fig. S7). In order to help to rationalize this process, Mössbauer spectra of a CO_2 treated sample (BCNF66) were recorded. Whereas the Mössbauer spectra of the as-prepared BCNFs in air showed the evidence Fe^{3+}, Fe^{4+} and Fe^{5+} ions, the BCNF66 sample heated under CO_2 showed that all the Fe^{5+} had been reduced to Fe^{3+}. In the Raman spectra, CO_2-treated BCNFs exhibited the peaks corresponding to graphitic-like carbon, carbonate and iron carbide. This indicates the possibility of the formation of $BaCO_3$ and Fe_2C as supported by PXRD data in Fig. S1B, SEM/EDX in Fig. S7 and the initial formation of carbonate groups seen in the *ab initio* calculations. As Fe^{3+} replaces Nb^{5+} with higher oxidation number (Fig. 4), Fe^{3+} adopts the surrounding environment by changing its oxidation state to 5+. As the samples are pre-treated with Ar gas, significant oxide ion vacancies are created owing to the reduction of the Fe^{5+}/Fe^{4+} component to Fe^{3+} (Fig. S8). These vacancy sites may act as centers to allow the adsorption of CO_2 from the gas feed. A number of perovskite oxides, particularly those containing Ba on the A-site, have been shown to exhibit strong propensity to accommodate.[40] The conversion of CO_2 to CO_3^{2-} would weaken the C-O bonds, and so might be the first step in the redox process that results in C formation. In this respect, electrons may have been donated from the BCNF-perovskite to reduce the CO_2 to C, with the oxide ions transiently accommodated in the BCNF lattice/surface oxide ion vacancies, being subsequently lost as O_2 under low $p(O_2)$ atmosphere. The higher level of C formation perhaps supports the importance of initial carbonate incorporation for BCNF100, where $BaCO_3$ impurities were observed on heating under pure CO_2 atmosphere (Fig. S1).

In general, the following reactions are thermodynamically viable and often used to show the CO_2 splitting process using reduced metal oxides (MOs)[14,18]:

$$\frac{1}{\delta} MO_x \rightarrow \frac{1}{\delta} MO_{x-\delta} + \frac{1}{2} O_{2(g)} \quad (1)$$

$$CO_{2(g)} + \frac{1}{\delta} MO_{x-\delta} \rightarrow \frac{1}{\delta} MO_x + CO_{(g)} \quad (2)$$

The net reaction is: $CO_{2(g)} \rightarrow CO_{(g)} + \frac{1}{2} O_{2(g)}$ (3)

A subsequent possible reaction on C deposition by using metal oxide, in particular iron oxides, has also been explored Tamaura *et al.*[17]

$$Fe_3O_4 + H_2 \rightarrow 3FeO + H_2O_{(g)} \quad (4)$$

$$3FeO + CO_{2(g)} \rightarrow Fe_3O_4 + C_{(s)} + \frac{1}{2} O_2 \quad (5)$$

The net reaction in this case is: $CO_{2(g)} \rightarrow C_{(g)} + O_{2(g)}$ (6)

In the present study, we believe that Fe sites may have been involved in a redox reaction under the continuous flow (100 sccm) of Ar for 12 h (Fig. S8), which can be expressed as:

$$O_O^x + 2Fe_{Fe}^{\times} \rightarrow V_O^{\cdot\cdot} + 2Fe_{Fe}^{'} + 0.5O_2 \quad (7)$$

The formation of carbon upon exposure to CO_2 can be expressed using the chemical reaction.

$$0.5CO_2 + V_O^{\cdot\cdot} + 2Fe_{Fe}^{'} \rightarrow 0.5C + 2Fe_{Fe}^{x} + O_o^x \quad (8)$$

Based on DFT calculations of various arrangements of cations on the surface, it is found that an Fe-rich and Nb-depleted surface with Ca:Nb:Fe = 1:0:3 is more stable when compared to surfaces with compositions approximating the bulk composition. A surface fully occupied by Fe

is, on the other hand, very unstable and tends to restructure (Table S3). We calculated the dependence of charge distribution on oxygen deficiency to investigate the possible oxidation state of Fe ions. As expected, it is the charge of Fe ions that varies strongly with the concentration of oxygen vacancies, while charges of other cations are less affected. On the other hand, for intermediate Fe ion charges, we observe an abrupt peak in the standard error of charge distribution on Fe that may indicate a tendency to split into high and low charges qualitatively in line with Mössbauer data. A quantitative comparison appears not possible, as the size of the employed structure models does not allow us to precisely reproduce the experimental nonstoichiometries.

Compared to defect-free surfaces, surfaces containing vacancies are more stable with respect to O_2 (Fig. 6 and Table S4). Computations of the adsorption process of CO_2 to various surfaces show that, except for the formation of a CO_3^{2-} group, the most stable configuration involves the formation of a 2O-C-Fe trigonal planar configuration with ΔE = -1.140 eV (Fig. 6). Removing O from this configuration is not favorable because it requires higher energy (ΔE = 1.617 eV). Considering this, the Fe-C bond can be formed energetically; however, the decomposition of such absorbed CO_2 is still a subject of debate. In addition, the adsorption of 2 CO_2 molecules on same Fe-site is unlikely to occur due to the high associated $\Delta E \sim 4.089$ eV compared to the adsorption energy of 2 CO_2 into 2 nearby vacancies ($\Delta E \sim 0.358$ eV). To conclude, the dissociation of CO_2 molecules into solid C can be summarized as following;

- Whether the concentration of CO_2 is in ppm or %, the formation of carbon was inevitable in Fe-doped BCNFs.

- The presence of oxygen vacancies on the surfaces and the adsorption of CO_2 near Fe on such surfaces are thermodynamically preferred.

- The dissociation of CO_2 and the strong interaction of Fe-C may lead to the addition of extra oxide ions into the BCNF, where BCNF being MIEC could eventually increase the total conductivity.[26]

The above results are highly significant as there have only been a few reports from early 1990 on CO_2 to C, CO, and O_2 conversion using activated magnetite[17,41] and transition metal-doped ferrites,[42-44] but no studies have been reported on the direct CO_2 thermal-decomposition to elemental carbon using a material with the double-perovskite structure. Nevertheless, Mn-based perovskites have been extensively explored for the solar-driven thermochemical generation of synthetic gas. [15,45] The high oxygen exchange capacity of Mn-based perovskites has made them attractive to enhance the process efficiency ($\eta_{solar\text{-}to\text{-}fuel}$) at lowers the temperature (~1200 °C vs. ~1500 °C of ceria).[46-48] Also, Ni and Co-doped ferrites have also been studied to decrease the temperature (<1000 °C) for the reduction of metal oxide, which subsequently improve the efficiency of solar thermochemical CO_2-splitting.[49,50] Furthermore, CO_2 to C and CO conversion using oxygen-deficient magnetite involved an essential initial step where H_2 is used in all cases to reduce the material first.[17,42,43,51,52] In contrast, our method directly converted CO_2 into C in one experimental step without any pre-treatment with expensive gaseous species such as H_2. Furthermore, the evolution of CO gas along with C formation provides the possibility to develop the materials for carbon-neutral synthetic fuel production with additional reactants (e.g., H_2O, H_2) in place with CO_2, utilizing renewable-energy for heating the system to the operating temperature.

4. Conclusions

Carbon build-up on Fe-doped perovskite was observed and confirmed using scanning electron microscopy (SEM) and energy dispersive X-ray analysis (EDX) studies on pre-treated (Ar, 700 °C) BCNFs. The thermal conductivity detector (TCD) signals using temperature programmed oxidation and mass spectra (TPO-MS) method added further evidence on the presence of carbon by heating the CO_2 pre-treated BCNF samples up to 900 °C and measuring the MS signals simultaneously. The lack of any solid carbon deposition on samples without Fe confirmed Fe's importance on the CO_2 reduction process. The creation of oxygen vacancies in BCNF by Fe-doping and its effect on the carbon formation was also discussed, and it is proposed that the changes in oxidation states with respect to changes in oxygen vacancy levels in these nonstoichiometric perovskites are key steps in the process. The C coating may provide a promising feature of these materials that could be used on their own at relatively low temperature (*i.e.* without Ni or any other catalysts that are employed with conventional higher temperature CeO_2 systems). In addition to the utilization of a combination of reactants, H_2 and/or H_2O, with CO_2 for low-energy intensive renewable-derived fuel production with these perovskite-based materials, which warrants further research.

Author Contribution

S.M. synthesis, experiments, data analysis and manuscript writing; C.H. & S.A. *ab* initio calculations, data analysis; A.H. TPO and MS experiments, data analysis; J. F. M. Mössbauer spectroscopy; P. R. S. & F. J. B. Mössbauer spectroscopy, data analysis; F.S. & E.R. Raman Spectroscopy; V.T. experimental design, data analysis, manuscript writing; All authors reviewed the manuscript.

Acknowledgements

This work was supported by the National Resources Canada and Carbon Management Canada (NRC-CMC) and the Natural Sciences and Engineering Research Council of Canada (NSERC) through discovery grants to V. T (Award number: RGPIN-2016-03853). Both S.M. and V.T. thank Professor David B. Layzell, Executive Director of ISEEE (Institute for Sustainable Energy, Environment and Economy) at the University of Calgary for his continuous encouragement. Authors are very thankful to Dr. Pedro Pereira Almao for the use of TPO-MS instrument. S.M. also thanks the Alberta Innovates Technology Futures (AITF) for a graduate scholarship. S.A. and H.C. are grateful to the Singapore National Research Foundation, Prime Minister's Office, who provided computational facilities and a scholarship to H.C. within the frame of Competitive Research Program awards NRF-CRP 10-2012-6 and NRF-CRP 8-2011-4. We also thank the Spanish MINECO for financial support through project MAT2015-64110-C2-1-P.

Notes and references

1. Y. Hori, A. Murata, K. Kikuchi, S. Suzuki, *J. Chem. Soc., Chem. Commun.* 1987, 728-729.

2. S. Ikeda, T. Takagi, K. Ito, *Bull. Chem. Soc. Jpn.* 1987, **60**, 2517-2522.

3. F. Studt, I. Sharafutdinov, F. Abild-Pedersen, C. F. Elkjær, J. S. Hummelshøj, S. Dahl, I. Chorkendorff, J. K. Nørskov, *Nat Chem* 2014, **6**, 320-324.

4. C.-W. Tsai, H. M. Chen, R.-S. Liu, K. Asakura, T.-S. Chan, *The Journal of Physical Chemistry C* 2011, **115**, 10180-10186.

5. V. S. K. Yadav, M. K. Purkait, *Energy & Fuels* 2015, **29**, 6670-6677.

6. S. Bontemps, L. Vendier, S. Sabo-Etienne, *J. Am. Chem. Soc.* 2014, **136**, 4419-4425.

7. R. Schlögl, *Angew. Chem. Int. Ed.* 2011, **50**, 6424-6426.

8. E. E. Benson, C. P. Kubiak, A. J. Sathrum, J. M. Smieja, *Chem. Soc. Rev.* 2009, **38**, 89-99.

9. Y. Chen, C. W. Li, M. W. Kanan, *J. Am. Chem. Soc.* 2012, **134**, 19969-19972.

10. C. W. Li, J. Ciston, M. W. Kanan, *Nature* 2014, **508**, 504-507.

11. C. W. Li, M. W. Kanan, *J. Am. Chem. Soc.* 2012, **134**, 7231-7234.

12. Y. Chen, M. W. Kanan, *J. Am. Chem. Soc.* 2012, **134**, 1986-1989.

13. W. C. Chueh, S. M. Haile, *ChemSusChem* 2009, **2**, 735-739.

14. W. C. Chueh, S. M. Haile, *Philosophical Transactions: Mathematical, Physical and Engineering Sciences* 2010, **368**, 3269-3294.

15. A. H. McDaniel, E. C. Miller, D. Arifin, A. Ambrosini, E. N. Coker, R. O'Hayre, W. C. Chueh, J. Tong, *Energy & Environmental Science* 2013, **6**, 2424-2428.

16. A. H. McDaniel, A. Ambrosini, E. N. Coker, J. E. Miller, W. C. Chueh, R. O'Hayre, J. Tong, *Energy Procedia* 2014, **49**, 2009-2018.

17. Y. Tamaura, M. Tahata, *Nature* 1990, **346**, 255-256.

18. W. C. Chueh, C. Falter, M. Abbott, D. Scipio, P. Furler, S. M. Haile, A. Steinfeld, *Science* 2010, **330**, 1797-1801.

19. L. J. Venstrom, R. M. De Smith, Y. Hao, S. M. Haile, J. H. Davidson, *Energy & Fuels* 2014, **28**, 2732-2742.

20. G. Kresse, J. Furthmüller, *Computational Materials Science* 1996, **6**, 15-50.

21. J. P. Perdew, K. Burke, M. Ernzerhof, *Phys. Rev. Lett.* 1996, **77**, 3865-3868.

22. V. I. Anisimov, J. Zaanen, O. K. Andersen, *Physical Review B* 1991, **44**, 943-954.

23. F. Zhou, M. Cococcioni, C. A. Marianetti, D. Morgan, G. Ceder, *Physical Review B* 2004, **70**, 235121.

24. K. W. Lee, W. E. Pickett, *Physical Review B* 2015, **91**, 195152.

25. K. W. Lee, J. Kuneš, R. T. Scalettar, W. E. Pickett, *Physical Review B* 2007, **76**, 144513.

26. S. Mulmi, V. Thangadurai, *J. Electrochem. Soc.* 2013, **160**, B95-B101.

27. S. Mulmi, A. Hassan, P. Pereira-Almao, V. Thangadurai, *Sensors and Actuators B: Chemical* 2013, **178**, 598-605.

28. B. Kitiyanan, W. E. Alvarez, J. H. Harwell, D. E. Resasco, *Chem. Phys. Lett.* 2000, **317**, 497-503.

29. P. Adler, *J. Solid State Chem.* 1997, **130**, 129-139.

30. S. E. Dann, M. T. Weller, D. B. Currie, M. F. Thomas, A. D. Al-Rawwas, *J. Mater. Chem.* 1993, **3**, 1231-1237.

31. G. Simon Case, A. L. Hector, W. Levason, R. L. Needs, M. F. Thomas, M. T. Weller, *J. Mater. Chem.* 1999, **9**, 2821-2827.

32. G. Demazeau, P. Fabritchnyi, L. Fournes, S. Darracq, I. A. Presniakov, K. V. Pokholok, V. P. Gorkov, J. Etourneaua, *J. Mater. Chem.* 1995, **5**, 553-556.

33. F. J. Berry, F. B. Andrew, C. C. Fiona, D. J. Simon, A. M. Elaine, P. R. Slater, F. T. Michael, J. W. Adrian, R. Xiaolin, *J. Phys.: Condens. Matter* 2009, **21**, 256001.

34. J. M. Porras-Vazquez, T. Pike, C. A. Hancock, J. F. Marco, F. J. Berry, P. R. Slater, *Journal of Materials Chemistry A* 2013, **1**, 11834-11841.

35. F. Menil, *J. Phys. Chem. Solids* 1985, **46**, 763-789.

36. F. Tuinstra, J. L. Koenig, *The Journal of Chemical Physics* 1970, **53**, 1126-1130.

37. Y. Wang, D. C. Alsmeyer, R. L. McCreery, *Chem. Mater.* 1990, **2**, 557-563.

38. A. C. Ferrari, J. Robertson, *Physical Review B* 2000, **61**, 14095-14107.

39. L. F. Maia, R. F. Fernandes, G. Lobo-Hajdu, L. F. C. de Oliveira, *Philosophical Transactions of the Royal Society of London A: Mathematical, Physical and Engineering Sciences* 2014, **372**, 1-11.

40. C. A. Hancock, J. M. Porras-Vazquez, P. J. Keenan, P. R. Slater, *Dalton Transactions* 2015, **44**, 10559-10569.

41. M. Tsuji, T. Togawa, Y. Wada, T. Sano, Y. Tamaura, *J. Chem. Soc., Faraday Trans.* 1995, **91**, 1533-1538.

42. H. Kato, T. Kodama, M. Tsuji, Y. Tamaura, S. G. Chang, *Journal of Materials Science* 1994, **29**, 5689-5692.

43. M. Tabata, H. Kato, T. Kodama, T. Yoshida, M. Tsuji, Y. Tamaura, *Journal of Materials Science* 1994, **29**, 999-1003.

44. T. Kodama, M. Tabata, K. Tominaga, T. Yoshida, Y. Tamaura, *Journal of Materials Science* 1993, **28**, 547-552.

45. J. R. Scheffe, D. Weibel, A. Steinfeld, *Energy & Fuels* 2013, **27**, 4250-4257.

46. J. R. Scheffe, A. Steinfeld, *Mater. Today* 2014, **17**, 341-348.

47. S. Dey, C. N. R. Rao, *ACS Energy Letters* 2016, **1**, 237-243.

48. S. Dey, B. S. Naidu, C. N. R. Rao, *Chemistry – A European Journal* 2015, **21**, 7077-7081.

49. K. M. Allen, N. Auyeung, N. Rahmatian, J. F. Klausner, E. N. Coker, *JOM* 2013, **65**, 1682-1693.

50. A. Singh, F. Al-Raqom, J. Klausner, J. Petrasch, *Int. J. Hydrogen Energy* 2012, **37**, 7442-7450.

51. M. Tabata, Y. Nishida, T. Kodama, K. Mimori, T. Yoshida, Y. Tamaura, *Journal of Materials Science* 1993, **28**, 971-974.

52. K. Akanuma, K. Nishizawa, T. Kodama, M. Tabata, K. Mimori, T. Yoshida, M. Tsuji, Y. Tamaura, *Journal of Materials Science* 1993, **28**, 860-864.

Figures

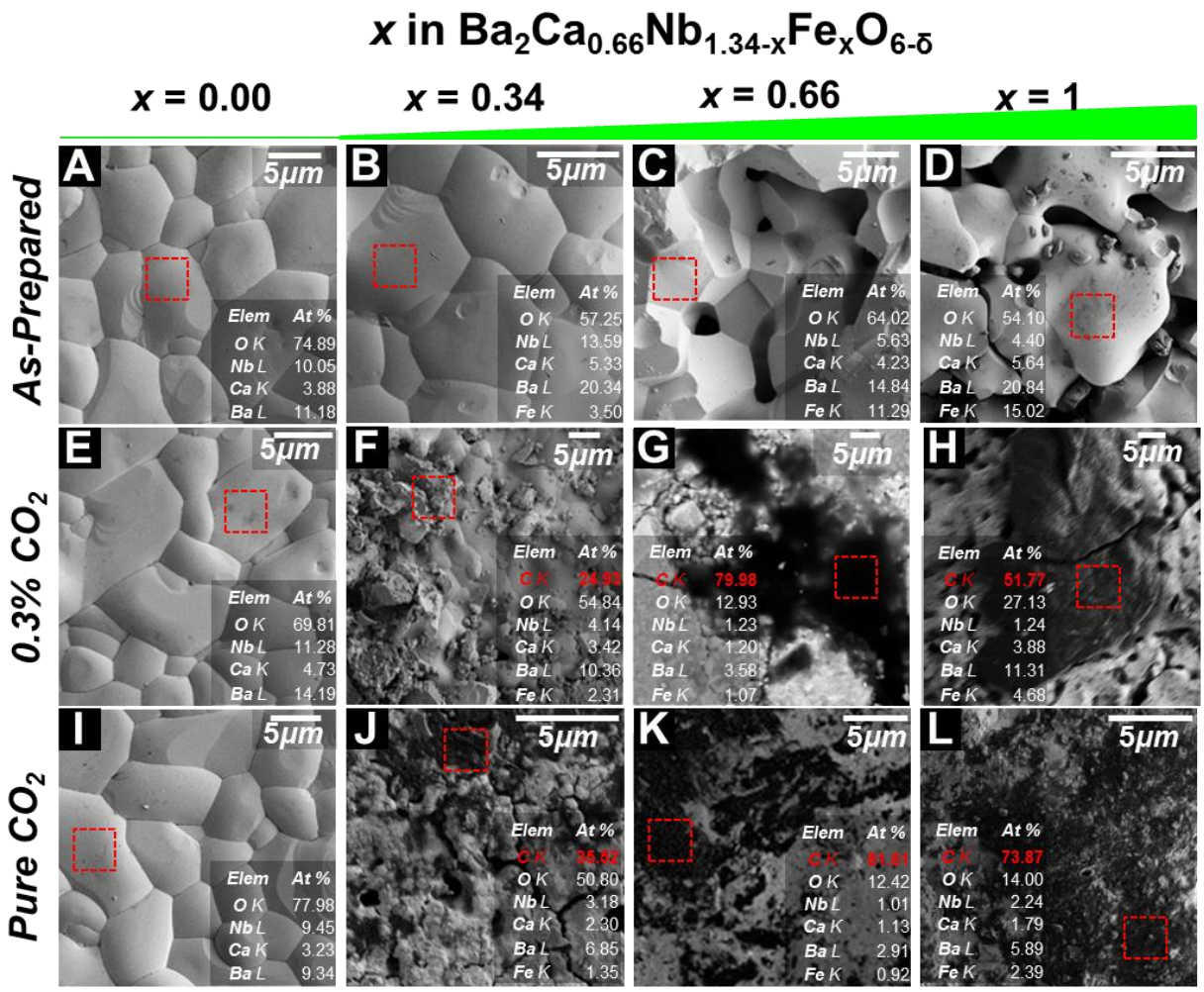

Figure 1. Typical SEM images of as-prepared $Ba_2Ca_{0.66}Nb_{1.34-x}Fe_xO_{6-\delta}$ with (A) x = 0, (B) x = 0.34, (C) x = 0.66 and (D) x = 1; 0.3% CO_2/Ar treated $Ba_2Ca_{0.66}Nb_{1.34-x}Fe_xO_{6-\delta}$ with (E) x = 0, (F) x = 0.34, (G) x = 0.66 and (H) x = 1; pure CO_2-treated $Ba_2Ca_{0.66}Nb_{1.34-x}Fe_xO_{6-\delta}$ with (I) x = 0, (J) x = 0.34, (K) x = 0.66 and (L) x = 1. Box with red-dotted line shows the area where EDX is taken and data is presented on the corresponding image.

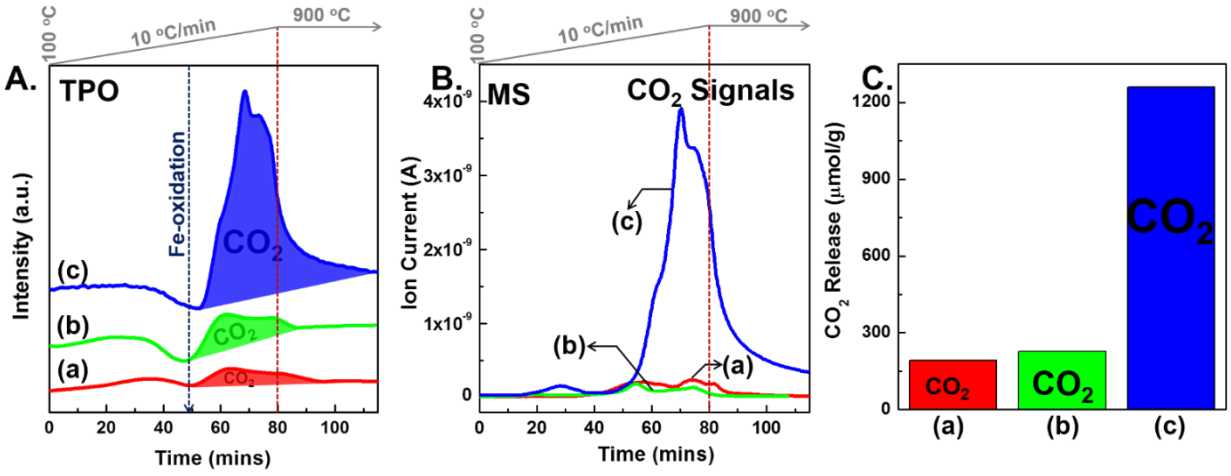

Figure 2. (A) Temperature programmed oxidation (TPO) profile of pure CO_2 pre-treated (700 °C, 24h) $Ba_2(Ca_{0.66}Nb_{1.34-x}Fe_x)O_{6-\delta}$, where (a) x = 0.34, (b) x = 0.66 and (c) x = 1, powder measured as a function of temperature using 5% O_2/He (ramping rate = 10 °C/min, total flow = 20 sccm); (B) Corresponding mass spectra (MS) of (a), (b) and (c) measured from the outlet of TPO in real-time; (C) Total CO_2 released calculated by integrating the area under the peak corresponding to CO_2 using (a), (b) and (c) in (A).

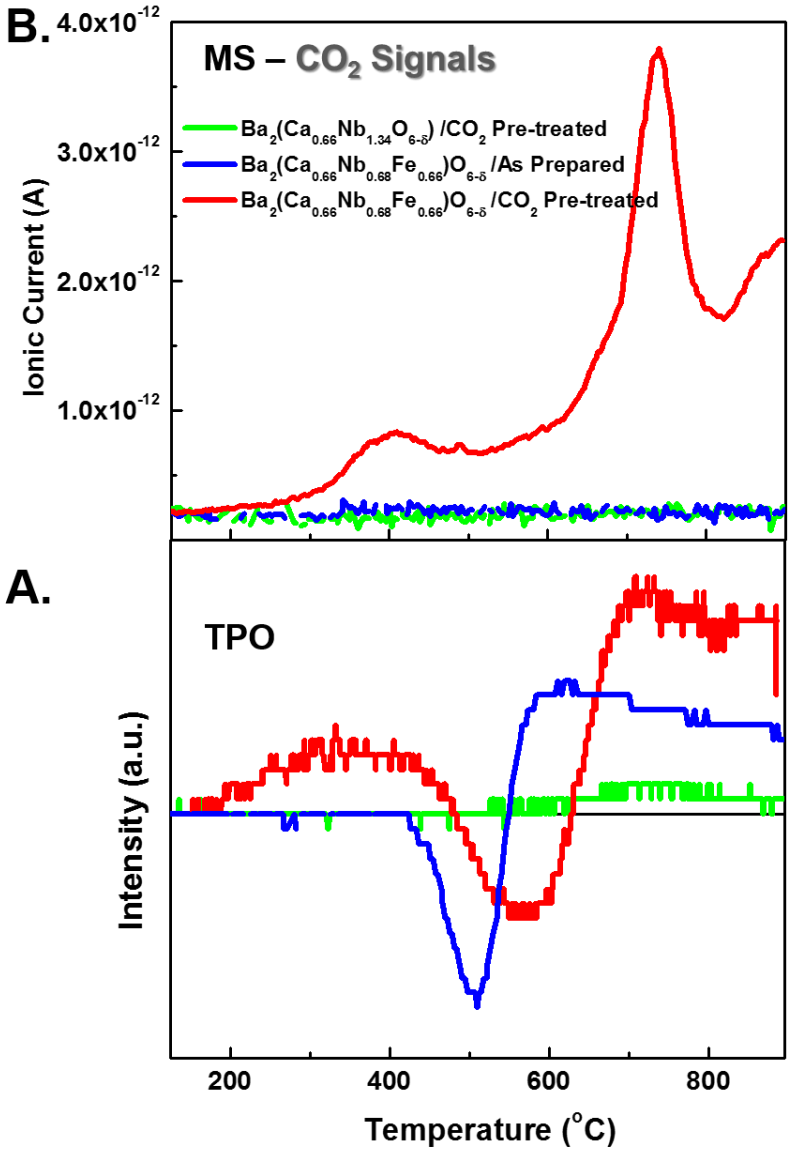

Figure 3. (A) Temperature programmed oxidation (TPO) profile of pure CO_2–treated (700 ^oC, 24h) Fe-free BCN (green), as-prepared Fe-doped BCNF66 (blue) and pure CO_2–treated (700 ^oC, 24h) BCNF66 (red) measured as a function of temperature using 5% O_2/ He (ramping rate = 10 ^oC/ min; total flow = 20 sccm); and (B) Corresponding mass spectra (MS) in real-time showing CO_2 signals. All samples were in powder form.

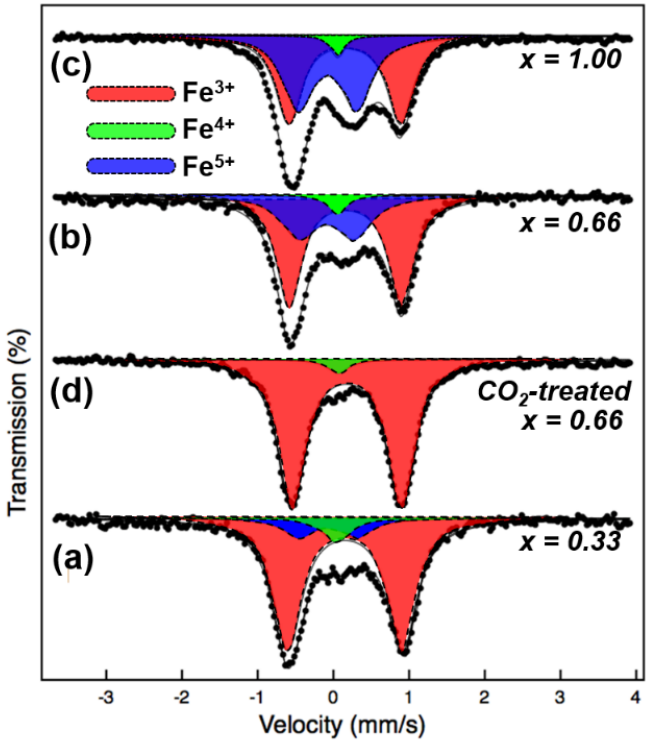

Figure 4. ^{57}Fe Mössbauer spectra recorded from as-prepared $Ba_2(Ca_{0.66}Nb_{1.34-x}Fe_x)O_{6-\delta}$, where (a) x = 0.34 (red), (b) x = 0.66 (green), (c) x = 1.00 (blue) and (d) pure CO_2-treated $Ba_2(Ca_{0.66}Nb_{1.34-x}Fe_x)O_{6-\delta}$, where x = 0.66 are best fitted to two quadrupole split absorptions together with a single line absorption of low intensity. The doublet with chemical isomer shift ca. -0.08 mm s^{-1} is characteristic of Fe^{5+} , while that at ca. 0.16 mm s^{-1} is typical of Fe^{3+} in perovskite-related structures. The singlet of low intensity with chemical isomer shift ca.0.05 mm s^{-1} can be associated with Fe^{4+}.

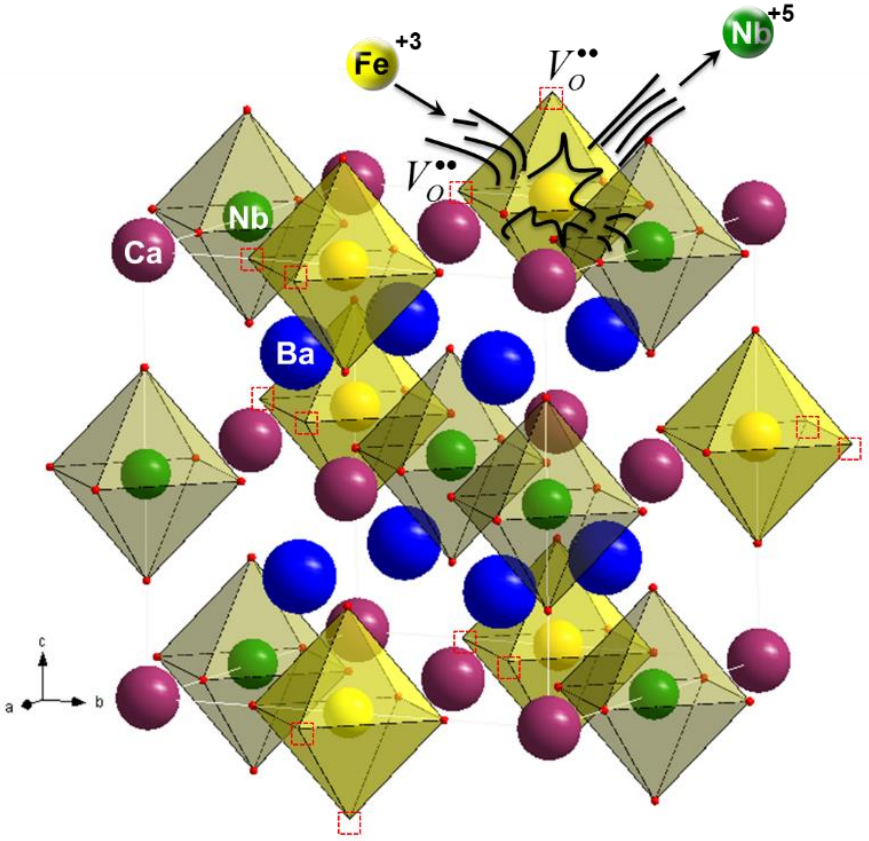

Figure 5. Schematic diagram of $Ba_2(Ca_{0.66}Nb_{1.34-x}Fe_x)O_{6-\delta}$ (BCNF) with theoretical lattice constant of a = 8 Å (space group *Fm-3m*, #225), where six Nb^{5+} atoms are replaced by six Fe^{3+} atoms creating two vacancy sites (in each FeO_6 octahedron) in Fe-doped sites denoted by red dotted boxes.

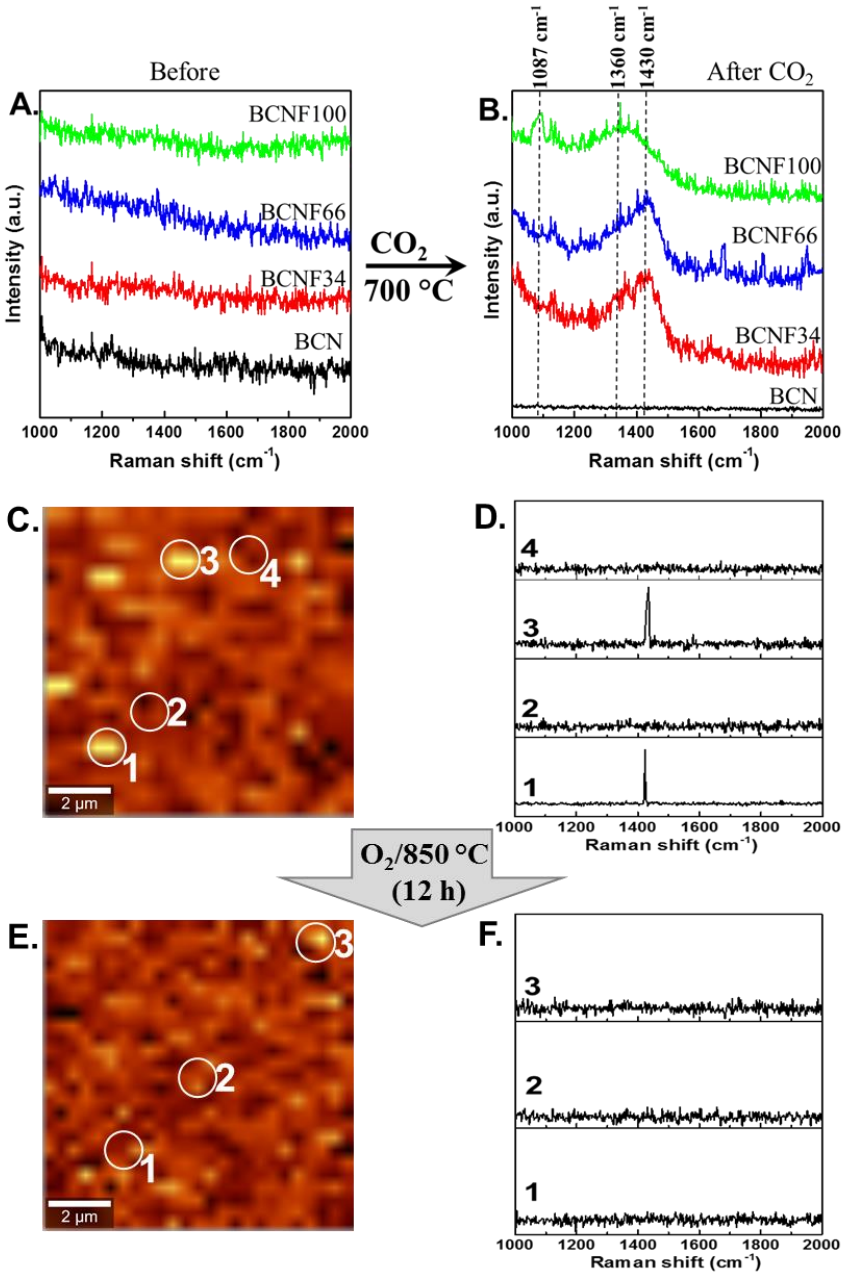

Figure 6. Raman spectra results of as-prepared BCN, BCNF34, BCNF66, and BCNF100 (A) before and (B) after CO_2-treatment at 700 °C for 24 h; (C) D-band Raman images of BCNF66 from (B); (D) The Raman spectra obtained in regions 1, 2, 3 and 4 (white circles) depicted in (C) are shown; (E) D-band Raman images of BCNF in (C) after oxidizing (with O_2) at 900 °C for 12 h; (F) The Raman spectra obtained in regions 1, 2 and 3 (white circles) depicted in (E) are shown.

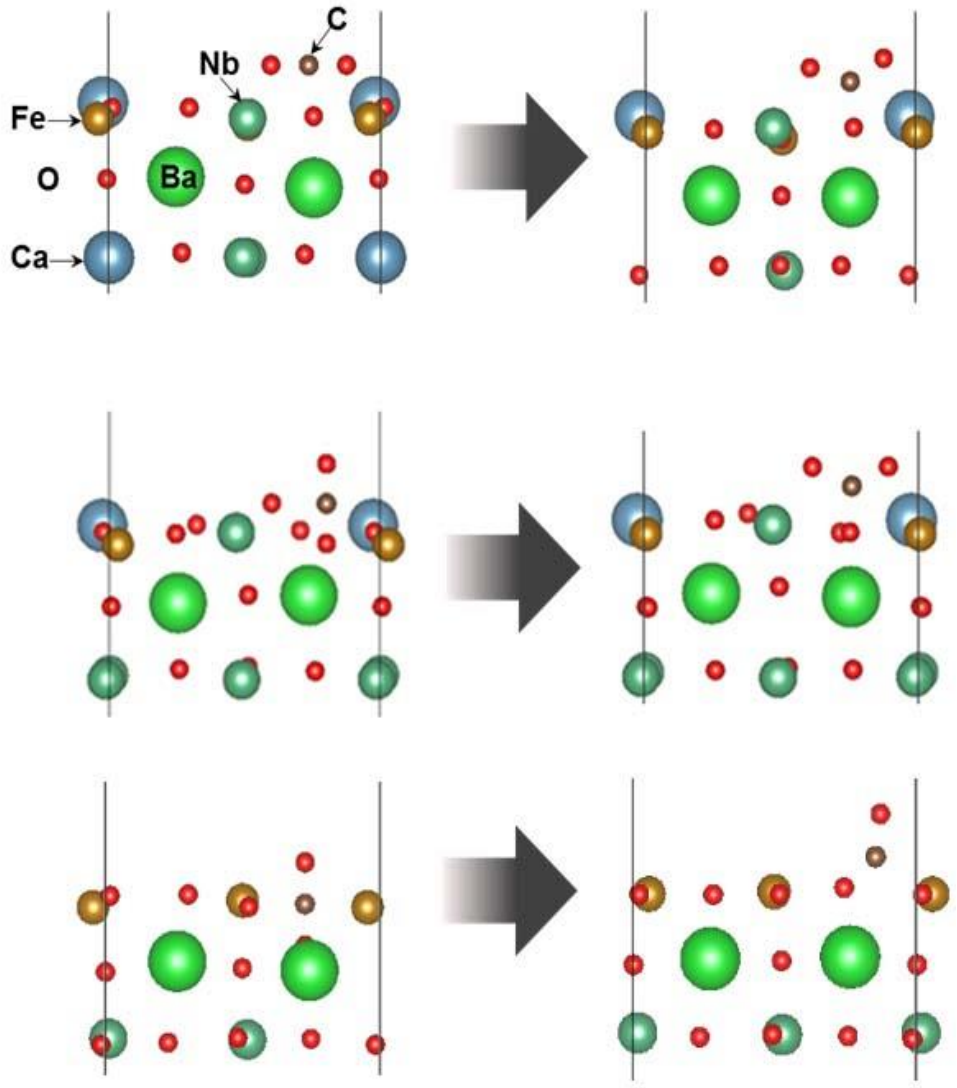

Figure 7. The energetically most favoured configuration for adsorption of CO_2 to the oxygen defect-free surface, F1 (top row, see Supporting Information Table S4), the most stable of the studied oxygen-defect containing surfaces, D1 (mid row, see also Table S4), and the formation of 2O-Fe-C group on Fe-rich surface D9 (bottom row, see also Table S4). In all cases the CO_2 molecule (left) is bent to form a trigonal planar group (right).